

Discrete element modeling of subglacial sediment deformation

Anders Damsgaard,¹ David L. Egholm,¹ Jan A. Piotrowski,¹ Slawek Tulaczyk,² Nicolaj K. Larsen,¹ and Karol Tylmann³

Received 17 April 2013; revised 4 September 2013; accepted 2 October 2013; published 18 October 2013.

[1] The Discrete Element Method (DEM) is used in this study to explore the highly nonlinear dynamics of a granular bed when exposed to stress conditions comparable to those at the bed of warm-based glaciers. Complementary to analog experiments, the numerical approach allows a detailed analysis of the material dynamics and the shear zone development during progressive shear strain. The geometry of the heterogeneous stress network is visible in the form of force-carrying grain bridges and adjacent, volumetrically dominant, inactive zones. We demonstrate how the shear zone thickness and dilation depend on the level of normal (overburden) stress, and we show how high normal stress can mobilize material to great depths. The particle rotational axes tend to align with progressive shear strain, with rotations both along and reverse to the shear direction. The results from successive laboratory ring-shear experiments on simple granular materials are compared to results from similar numerical experiments. The simulated DEM material and all tested laboratory materials deform by an elastoplastic rheology under the applied effective normal stress. These results demonstrate that the DEM is a viable alternative to continuum models for small-scale analysis of sediment deformation. It can be used to simulate the macromechanical behavior of simple granular sediments, and it provides an opportunity to study how microstructures in subglacial sediments are formed during progressive shear strain.

Citation: Damsgaard, A., D. L. Egholm, J. A. Piotrowski, S. Tulaczyk, N. K. Larsen, and K. Tylmann (2013), Discrete element modeling of subglacial sediment deformation, *J. Geophys. Res. Earth Surf.*, 118, 2230–2242, doi:10.1002/2013JF002830.

1. Introduction

[2] Deformation of subglacial sediment may be a major contributor to the overall movement of warm-based glaciers and ice streams [e.g., *Alley et al.*, 1986; *Boulton and Hindmarsh*, 1987; *Engelhardt et al.*, 1990; *Kamb*, 1991; *Boulton*, 1996], and it is also suspected to influence the periodic dynamics of surge-type glaciers [*Boulton and Jones*, 1979; *Clarke et al.*, 1984 *Evans and Rea*, 1999; *Murray et al.*, 2000, 2003]. In addition, subglacial deformation is sometimes regarded as the primary mechanism for sediment advection/discharge [e.g., *Kjær et al.*, 2006; *Nygård et al.*, 2007]. However, the physics of subglacial sediment deformation are still debated, and the deformation mode remains one of the most controversial elements of glacier dynamics [e.g., *Boulton and Hindmarsh*, 1987; *Hindmarsh*, 1998; *Fowler*, 2003; *Tulaczyk*, 2006; *Cuffey and Paterson*, 2010].

[3] Based on field measurements of deep sediment deformation, *Boulton and Hindmarsh* [1987] suggested that subglacial sediment behaves like a viscoplastic material. Viscoplastic continuum models have since been popular among computational ice sheet models [e.g., *Alley et al.*, 1987; *Hindmarsh*, 1998; *Fowler*, 2000; *Ng*, 2000], for which the rate-dependent viscous models offer a convenient one-to-one relationship between stress and strain rate. Contrasting this approach, *Schoof* [2006] described a possible implementation of a basal boundary condition with a plastic yield stress to glacial flow models. The coupled system of glacial hydrology and nonlinear basal sediment behavior has been reported to be of great importance for stick-slip events [*Bueler and Brown*, 2009; *Bougamont et al.*, 2011; *Bougamont and Christoffersen*, 2012].

[4] As noted by, e.g., *Kamb* [1991] and *Iverson* [2010], laboratory shear experiments on subglacial sediment do not confirm the rate-dependent viscous plastic model but instead indicate that subglacial sediment deforms due to Coulomb slip, independently of the applied strain rate. *Tulaczyk et al.* [2000] and *Iverson and Iverson* [2001] demonstrated that subglacial till, deforming according to the Mohr-Coulomb plastic rheology, may also produce the deep-seated deformation profiles that are observed in the field and often associated with a viscoplastic behavior.

[5] However, subglacial sediment is first and foremost a granular material with an inherent ability to change

¹Department of Geoscience, Aarhus University, Aarhus C, Denmark.

²Department of Earth and Planetary Sciences, University of California, Santa Cruz, California, USA.

³Department of Earth Sciences, N. Copernicus University, Toruń, Poland.

Corresponding author: A. Damsgaard, Department of Geoscience, Aarhus University, Høegh-Guldbergs Gade 2, 8000 Aarhus C, Denmark. (anders.damsgaard@geo.au.dk)

mechanical behavior, depending on the stress state, deformation rate, and pore water pressure. This study presents the first effort to apply the Discrete Element Method (DEM, also called the distinct element method) [Cundall and Strack, 1979] for studying the granular physics of subglacial till deformation. This method was first suggested in this context by Iverson and Iverson [2001] and Fowler [2003].

[6] We explore the applicability of the DEM as an alternative to the continuum-based visco-elastic-plastic methods for modeling subglacial deformation. A discrete modeling approach can capture the highly nonlinear dynamics of subglacial deformation, as demonstrated by laboratory shear experiments on subglacial sediment samples [Iverson et al., 1997; Tulaczyk, 1999; Thomason and Iverson, 2006; Rathbun et al., 2008; Iverson, 2010]. As a supplement to laboratory experiments, numerical modeling offers complete control over all model parameters, such as grain size distribution, geotechnical properties of the material, and boundary conditions. This facilitates a more transparent experimental setup whereby it is possible to repeat experiments and quantify the effects of all input parameters. The numerical approach allows a detailed analysis of the particle kinematics, during and after the experiment. This small-scale analysis exceeds the capacity of laboratory experiments, but the numerical experiments are, however, constrained by the number of particles and simplifying assumptions about the particle shapes.

[7] Here we first present previous studies on the topic of granular mechanics. We then describe the details of the applied numerical model, as well as the setup and results of shear experiments. We take a closer look at the internal characteristics of the shear zone from the numerical experiments and the implications for subglacial deformational processes. Finally, we compare the modeled macroscopical mechanical behavior to the results of laboratory ring-shear experiments on different granular materials.

2. Granular Mechanics During Shear

[8] In the field of glacial micromorphology, microscale deformation structures have been categorized as either brittle, ductile, or polyphase, suggesting a natural variability in the mode of deformation [van der Meer, 1993, 1996; Menzies, 2000; Larsen et al., 2006; Phillips et al., 2013; Vaughan-Hirsch et al., 2013]. Generally, the physical properties of granular materials cannot be fully described by ideal viscous or elastoplastic continuum relationships. Depending on the average kinematic energy of each grain or particle, a granular assemblage can assume properties of solid-like, fluid-like, or even gaseous states [e.g. Jaeger et al., 1996]. At rest, under the influence of gravity and confining stress, granular matter forms a stable packing and behaves like a solid, and the same material can take a range of packing densities, dependent on the style of deposition and the stress history [Herrmann, 2002]. Overall, the rheology of all dry granular materials is strain rate independent at low shearing velocities, where they deform in a pseudo static state. If granular materials deform under higher shearing velocities, particle inertia dominates and deformation becomes rate dependent (*Bagnold flow*) [Zang and Campbell, 1992; Campbell, 2006; Krimer et al., 2012]. In confined shear

experiments, the dimensionless inertia parameter I is defined by

$$I = \dot{\gamma} \bar{r} \sqrt{\frac{\rho}{\sigma_0}} \quad (1)$$

where $\dot{\gamma}$ is the shear strain rate, \bar{r} is the mean particle radius, ρ is the material density, and σ_0 is the magnitude of the normal stress [GDR-MiDi, 2004]. Experiments and simulations show that the material deforms in a pseudo static and rate-independent manner when $I < 10^{-3}$ [GDR-MiDi, 2004].

[9] Aharonov and Sparks [2002] conducted two-dimensional DEM simulations of shear experiments on granular material and recognized two different modes of strain localization, depending on the applied levels of shear velocity and normal stress. With relatively low normal stress and high shear velocity, the deformation was characterized by shallow deformation in a persistent boundary layer shear zone. In contrast, the deformation was deep and distributed for higher stress levels and lower shearing velocities.

[10] Reynolds [1885] and Mead [1925] recognized that initially consolidated, rigid granular materials, subjected to a shearing stress, require an increase in volume (dilatancy) to deform. When the shearing motion stops, the shear zone collapses and compacts due to the compressive stress. The shear strain is often localized in shear zones, which can have a range of sizes, dependent on the boundary conditions and material properties. The minimal thickness in noncohesive materials is in the order of 5–10 grain diameters [de Gennes, 1999]. Herrmann [2001] suggested a typical shear band thickness minimum, based on considerations of the force acting to mobilize particles. As a result of contact friction between neighboring particles, the magnitude of the mobilization force is inversely proportional to the distance along the stress-bearing force chains. This stabilizing effect causes the shear-induced particle velocity to decay exponentially with the distance from the center of the shear band.

[11] If elastic deformation is ignored, the behavior of granular materials (including tills) can be approximated by the Mohr-Coulomb failure criterion [e.g., Boulton and Jones, 1979; Nedderman, 1992; Hooke et al., 1997; Clarke, 2005; Iverson, 2010]. For Mohr-Coulomb materials, the macromechanical angle of internal friction (ϕ) and the cohesion (C) are defined from the linear representation of the value of the material *peak* or *ultimate* shear strength ($\tau_{p,u}$) under a range of normal stress magnitudes (σ_0):

$$\tau_{p,u} = C_{p,u} + \sigma_0 \tan(\phi_{p,u}) \quad (2)$$

Most materials can display a range of shear strengths, depending on the consolidation state. Consolidated materials in a prefailure state typically have a higher peak value of shear strength (τ_p) than materials in the *critical state* with a fully developed, active shear zone and a residual, ultimate shear strength (τ_u) [Schofield and Wroth, 1968; Atkinson and Bransby, 1979; Nedderman, 1992]. Similarly, the material cohesion can change during deformation. In particular, the peak cohesion is higher than the ultimate cohesion if the cohesive bonds between grains are not reestablished after breaking.

3. The Discrete Particle Model

[12] The Discrete Element Method was initially formulated by Cundall and Strack [1979]. The computational

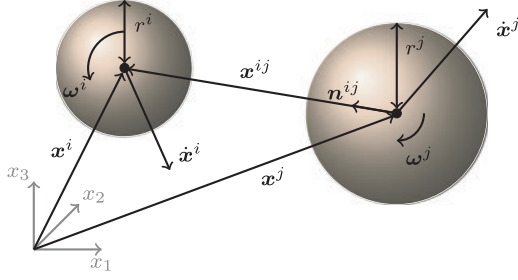


Figure 1. The DEM particles are represented by spheres with center position \mathbf{x} and radius r . The velocity vector of a particle is denoted by $\dot{\mathbf{x}}$, and the angular velocity vector is $\boldsymbol{\omega}$. A particle pair is characterized by the interparticle vector \mathbf{x}^{ij} and the contact normal vector \mathbf{n}^{ij} .

method simulates the physical behavior of discontinuous materials in a way that is ideal for reproducing the highly nonlinear dynamics of granular materials. The DEM has, in addition to geotechnical simulations [e.g., Cheng *et al.*, 2003; Potyondy and Cundall, 2004], already been used for simulating various sedimentological transport modes, such as debris flows [Yohannes *et al.*, 2012], bed load transport [Drake and Calantoni, 2001], aeolian saltation [Sun *et al.*, 2001], mechanical sorting [e.g., Rosato *et al.*, 2002; Kudrolli, 2004], as well as sandbox deformation experiments [Egholm *et al.*, 2007, 2008] and mechanical properties of fault gouges in the earthquake generation process [e.g., Morgan and Boettcher, 1999; Morgan, 1999, 2004; Mair and Abe, 2008].

[13] The DEM simulates the micromechanical behavior and interaction of discrete, unbreakable particles with their own mass and inertia, under the influence of, e.g., gravity and boundary conditions such as moving walls. The particulate nature of the DEM is optimal not only for capturing the discrete nature of granular physics but also for simulating the large strains observed in soft subglacial beds. In contrast, mesh-based continuum numerical methods (e.g., the finite element method, the finite difference method, and the finite volume method) cannot simulate high deformation without frequent remeshing, which is often a very complicated and computationally expensive task. Additionally, the shear zone dynamics in standard continuum plasticity models are often affected by the grid resolution and the mesh-line orientation [Rudnicki and Rice, 1975; de Borst, 1991].

[14] The DEM includes deformation-induced porosity changes as an inherent property because, like true sediment grains, model particles must move past each other. In addition, the DEM responds naturally with granular-style deformation patterns, which can take place in a distributed manner over larger parts of the volume or in localized shear zones.

[15] In the applied DEM formulation, the particles are represented as spheres, which reduces the complexity of the contact search and dynamics. The geometric extent of each particle is represented by a position vector \mathbf{x} , and a radius r . Each particle has individual kinematic attributes, as illustrated in Figure 1. Based on the net force acting on each particle, the resulting movement is calculated in every small time step (Δt) by application of Newton's law of motion for particles of constant mass. For a particle i with n_c

contacts, the sums of translational and rotational forces are expressed by

$$m^i \dot{\mathbf{x}}^i = m^i \mathbf{g} + \underbrace{\sum_j^{n_c} (\mathbf{f}_n^{ij} + \mathbf{f}_t^{ij})}_{\text{Sum of translational forces}} \quad (3)$$

$$I^i \dot{\boldsymbol{\omega}}^i = \underbrace{\sum_j^{n_c} \left(- (r^i + 0.5 \delta_n^{ij}) \mathbf{n}^{ij} \times \mathbf{f}_t^{ij} \right)}_{\text{Sum of torques}} \quad (4)$$

where m is the particle mass, \mathbf{g} is the gravitational force vector, I is the moment of inertia, and $\boldsymbol{\omega}$ is the angular velocity. A dot denotes time derivation and a bold formatted symbol represents a three-dimensional vector.

[16] A particle is in contact with another particle or a wall if the volumes overlap. For a pair of spherical particles, hereafter denoted with superscripts i and j , the contact search is a simple operation, involving only the particle center coordinates and radii. The particle overlap is

$$\delta_n^{ij} = \|\mathbf{x}^{ij}\| - (r^i + r^j) \quad (5)$$

where $\mathbf{x}^{ij} = \mathbf{x}^i - \mathbf{x}^j$ is the interparticle vector. Particles overlap when $\delta_n^{ij} < 0$, in which case the force components normal (\mathbf{f}_n) and tangential (\mathbf{f}_t) to the contact plane are assumed to obey a conventional linear-elastic contact model (Figure 2):

$$\mathbf{f}_n^{ij} = -k_n \delta_n^{ij} \mathbf{n}^{ij} \quad \text{and} \quad \mathbf{f}_t^{ij} = -k_t \boldsymbol{\delta}_t^{ij} \quad (6)$$

where $\mathbf{n}^{ij} = \mathbf{x}^{ij} / \|\mathbf{x}^{ij}\|$ is the contact normal vector. k_n and k_t are the linear-elastic (Hookean) spring coefficients. The tangential displacement along the contact plane ($\boldsymbol{\delta}_t^{ij}$) is calculated incrementally by temporal integration of the tangential contact velocity and saved for the duration of the contact. The contact velocity $\boldsymbol{\delta}$ is found from the translational and rotational velocities of the particles in contact [Hinrichsen and Wolf, 2006]:

$$\boldsymbol{\delta}^{ij} = (\dot{\mathbf{x}}^i - \dot{\mathbf{x}}^j) + r^i (\mathbf{n}^{ij} \times \boldsymbol{\omega}^i) + r^j (\mathbf{n}^{ij} \times \boldsymbol{\omega}^j) \quad (7)$$

The contact velocity is further decomposed into normal ($\boldsymbol{\delta}_n$) and tangential ($\boldsymbol{\delta}_t$) components. The magnitude of the

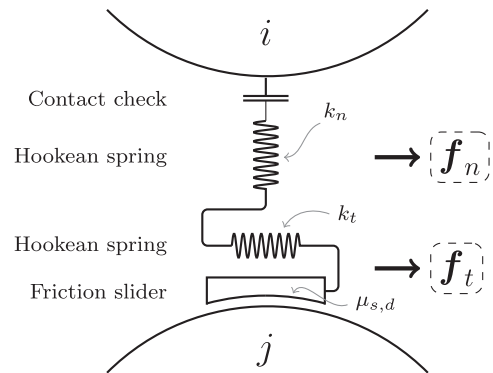


Figure 2. Schematic representation of the contact model components, normal and tangential to the contact plane.

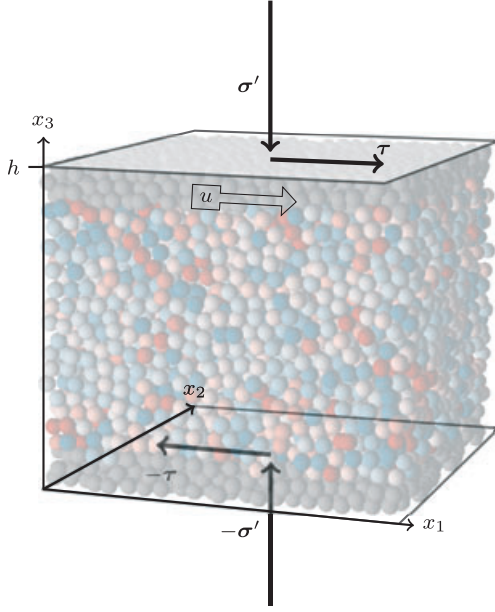


Figure 3. Model geometry in the numerical shear experiments. Grey particles have a fixed horizontal velocity; zero for the lower particles and u for the upper particles. The resultant shear stress (τ) is a function of the time (t), the shear velocity (u), the effective normal stress (σ'), the material stiffnesses ($k_{n,t}$), and the coefficients of friction ($\mu_{s,d}$). The boundaries to the left, right, front, and back are periodic.

tangential force is limited by the Coulomb-friction criterion of static and dynamic friction:

$$\|\mathbf{f}_t^{ij}\| \leq \begin{cases} \mu_s \|\mathbf{f}_n^{ij}\| & \text{if } \|\dot{\delta}_t\| = 0 \\ \mu_d \|\mathbf{f}_n^{ij}\| & \text{if } \|\dot{\delta}_t\| > 0 \end{cases} \quad (8)$$

where the static friction coefficient (μ_s) is larger or equal to the dynamic friction coefficient (μ_d). If the tangential force exceeds the static friction, the contact starts to slip along the contact plane. Strain-softening behavior at the contact can be introduced by having a lower dynamic than static friction coefficient value.

[17] The macroscopic geotechnical behavior of the simulated particle assemblage is generally a result of the self-organizing complexity of the particles, but it is influenced by the micromechanical parameters. As demonstrated by *Belheine et al.* [2009], the normal and shear stiffnesses ($k_{n,t}$) effectively control Young's modulus and Poisson's ratio, which are macroscopic parameters. The friction coefficients ($\mu_{s,d}$) control the level of dilatancy during deformation, which in turn governs the shear strength.

[18] Our DEM implementation is three-dimensional. This allows for particle rotation around arbitrary axes, which facilitates particle interlocking and gives a realistic three-dimensional geometry of the interparticle voids. Two-dimensional DEM models tend to overfacilitate particle rolling [e.g., *Morgan*, 1999], since the rotational axes of particles are always parallel. The enhanced rolling in a 2-D setup ultimately results in low shear strengths of the material.

[19] The kinematic grain behavior is time integrated in a fully explicit manner, resulting in a simple three-step algorithm:

[20] 1. Contact search (equation (5)): Interparticle and wall-particle contacts are identified.

[21] 2. Interaction (equations (6), (7), and (8)): For each particle contact, the contact forces and rotational moments are calculated.

[22] 3. Integration (equations (3) and (4)): Particle kinematics are updated using the sum of forces and torques, and time is increased by Δt .

[23] For the temporal integration, a second-order half-step leapfrog Verlet integration scheme is used [*Fraige and Langston*, 2004; *Krugger-Emden et al.*, 2008]. The length of the time step must be small enough to allow multiple updates of the kinematics, while the elastic wave travels through even the smallest particle in the assemblage. We therefore define the time step value on the basis of the natural undamped frequency ($\omega_0 = \sqrt{k/m}$) in a linear spring system ($\Delta t_{\text{crit}} = 2/\omega_0$) [*O'Sullivan and Bray*, 2004], which is a function of the elastic P wave velocity (v_p):

$$\Delta t = f \sqrt{\frac{\min(m)}{\max(k_n, k_t)}} = f \frac{\min(r) \sqrt{\frac{28}{9} m^{-1} \pi \min(r)}}{v_p} \quad (9)$$

where $\min(m)$ is the smallest particle mass and $\min(r)$ is the smallest particle radius. The constant f is introduced as a safety factor to account for the irregular contact network. It generally depends on the packing and the particle size distribution. In our experiments, a value of $f = 0.075$ was used [*Zhang and Campbell*, 1992].

[24] To cope with the high-computational requirements, the algorithm is formulated for graphics-processing unit computation using the CUDA C API [*Kirk and Hwu*, 2010; *NVIDIA*, 2013a, 2013b]. The sphere DEM software is a free and open-source software, licensed under the GNU Public License v. 3 (<https://gnu.org/licenses/gpl.html>). The project is maintained at <https://github.com/anders-dc/sphere>.

3.1. Model Configuration

[25] We have adapted a model geometry where infinite shear strains can be obtained with periodic lateral boundaries (Figure 3). When a particle moves across a periodic boundary, it immediately re-enters through the opposite side. The particle contact search also works across these boundaries,

Table 1. Micromechanical Properties and Geometrical Values for Particles in the DEM Shear Experiment

Parameter	Symbol	Value
Particle count	N	10,000
Mean diameter	$2\bar{r}$	0.04 m
Standard deviation of diameter	σ	0.000187 m
Spatial domain dimensions	\mathbf{L}	$0.86 \times 0.86 \times 0.94$ m
Material density	ρ	2.6×10^3 kg m ⁻³
Normal stiffness	k_n	1.16×10^9 Nm ⁻¹
Tangential stiffness	k_t	1.16×10^9 Nm ⁻¹
Friction coefficient (static)	μ_s	0.3
Friction coefficient (dynamic)	μ_d	0.3
Normal stress range	σ_0	10 to 120 kPa
Shear velocity	u	0.0369 ms ⁻¹
Wall mass	m_w	6.42 kg
Time step length	Δt	6.33×10^{-7} s
Simulation length	t_{total}	20 s

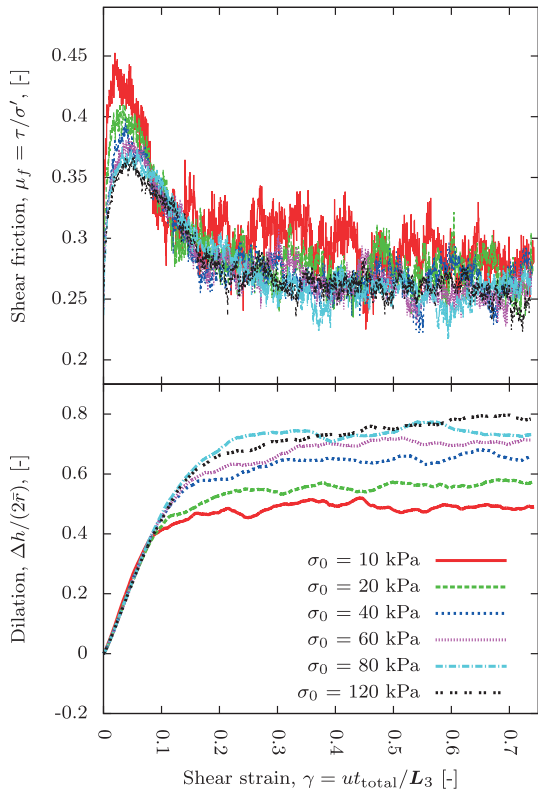


Figure 4. (top) Shear friction and (bottom) dilation as a function of shear strain, at different normal stress values in the DEM experiments.

so particle pairs can be in contact, although they are placed at opposite margins.

[26] The particles are initially positioned randomly but without particles in physical contact. The particle assemblage is then gravitationally consolidated by running the model through time, until the deficit potential energy, after temporarily being transformed to kinetic and rotational energy, is stored in the elastic components of the contacts or is dissipated away by the frictional components of the system. Next, the particles are subjected to consolidation under a normal stress (σ_0), applied to the dynamic top wall. The particles are afterward sheared at a constant velocity (u). The lowermost particles are fixed at their horizontal positions, while the uppermost particles are given a uniform, nonzero horizontal velocity. The fixed particles are defined to have a zero angular velocity. The shear stress (τ) and effective normal stress (σ') values are calculated as the sum of the force components acting on the upper fixed particles, along the axis of movement and normal to the top wall, respectively. The particle assemblage is free to dilate, as long as the upper stress boundary condition is satisfied. The numerical particles are indestructible, and the DEM experiments are therefore without grain crushing and abrasion.

[27] The values of the physical and geometrical parameters are listed in Table 1. For simplicity, equal values are used for the normal and tangential stiffnesses, as well as for the static and dynamical coefficients of friction. The particle radii are drawn from a log-normal distribution.

[28] The selected parameter values in the numerical experiments result in inertia parameter values

(I , equation (1)) between 7.5×10^{-4} and 2.2×10^{-4} . With these values, it is reasonable to assume that the material is deforming in a pseudo static state without significant effects of particle inertia. The shearing velocity exceeds the deformation rate under glaciers by several orders of magnitude, but since the material deforms rate independently beneath $I = 10^{-3}$, the larger velocity only helps to minimize the computational time required.

4. Results

[29] During the preshear consolidation phase, the numerical material compacts with exponentially decaying volumetric strain rates, which is typical for granular materials [Nedderman, 1992]. When sheared after consolidation, the numerical DEM material also behaves as a normally consolidated granular material, with clearly distinguishable peak and ultimate shear strength values (Figure 4). The peak and ultimate shear friction values depend on the level of normal stress. A high level of normal stress requires larger shear strains before the ultimate shear strength is reached. Furthermore, the magnitude of the total dilation increases with the magnitude of the normal stress.

[30] The Mohr-Coulomb relationship (equation (2)) is fitted to the shear stress data using a nonlinear least squares Marquardt-Levenberg algorithm. The regressed coefficients and their asymptotic standard error values are $\phi_p = 32^\circ \pm 0.31^\circ$, $C_p = 1.2 \pm 0.21$ kPa in the peak failure state and $\phi_u = 22^\circ \pm 0.47^\circ$ and $C_u = 0.51 \pm 0.31$ kPa in the critical failure state. The linear correlation confirms that the material deforms according to the Mohr-Coulomb theory. The measured values of the macromechanical angle of internal friction are within the range found in other tests involving real materials, ranging from 17° for smooth spherical particles to about 56° for angular particles [Nedderman, 1992].

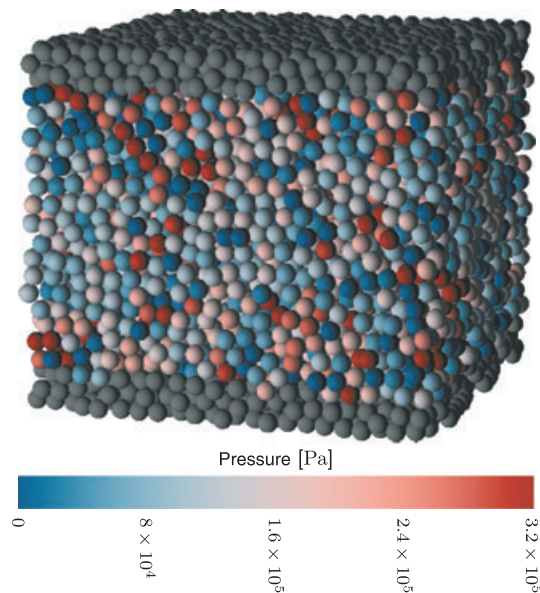


Figure 5. Visualization of the dispersive pressures of the heterogeneous stress network in the simulated material with $\sigma_0 = 80$ kPa.

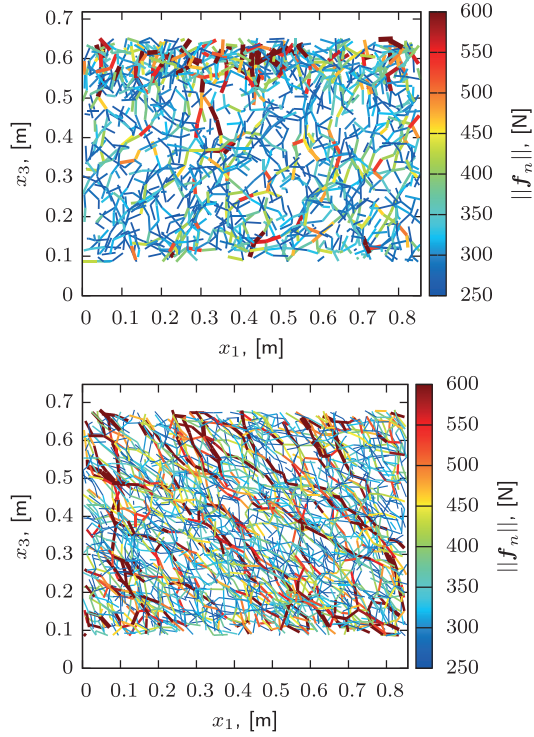


Figure 6. Force distribution in the nonfixed particles during (top) consolidation and during (bottom) shear. $\sigma_0 = 80$ kPa in both cases. The width and color of the line segments are determined by the magnitude of the contact normal force ($\|f_n\|$). The shear movement in the lower plot takes place along the top boundary toward the right. Several of the contacts forces are greatly exceeding the upper limit of the color bar.

[31] Within the modeled material, stress is distributed heterogeneously along a complex network of force chains (Figures 5 and 6). Particles in a force chain are often subjected to stress magnitudes more than 4 times the macroscopic confining stress (Figure 5). The force chains are generally aligned with the direction of maximum compressive

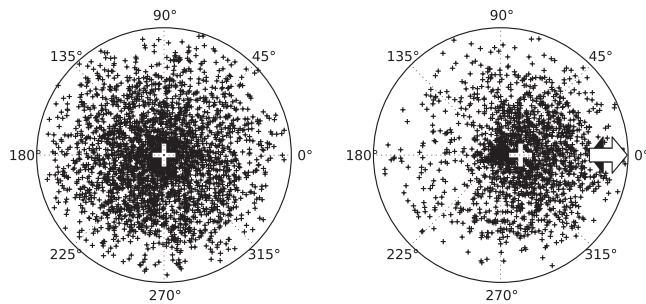


Figure 7. Trend and plunge of the 50% strongest DEM interparticle normal forces (f_n) during (left) consolidation and during (right) shear. $\sigma_0 = 80$ kPa in both cases. The plots are equal angle stereographic projections on the lower hemisphere, with the stereonet equator situated in the horizontal (x_1, x_2) plane. The white plus symbols denote the trend and plunge of the maximum compressive stress ($\sigma' + \tau$). The arrows in the right plot denote the shearing direction.

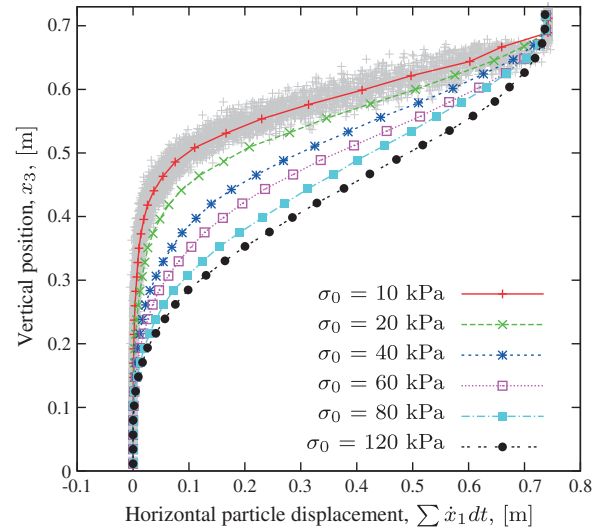


Figure 8. Laterally averaged strain-depth profiles at the end of the numerical DEM experiments with varying levels of overburden normal stress. The individual particle values for the $\sigma_0 = 10$ kPa experiment are underlain to visualize the horizontal variance of the displacement. The total shear distance is 0.738 m.

stress, resulting from the combined influence of the overburden normal stress and the shear movement (Figure 7). Therefore, force chains are predominantly vertical during consolidation and subhorizontal during shear. In the latter situation with shear, the force chain network is rapidly reconfiguring, even faster than the grain reorganization (A supplementary animation is available at: <http://users-cs.au.dk/adk/files/shear-80kPa-pressures.mp4> (29 MB)).

[32] In the absence of friction from the sides, the shear zone develops near the top boundary since this configuration requires a minimum of material to be accelerated. Furthermore, the material strengthens with depth because the weight of the overburden material increases the normal stress and the shear strength of particle contacts (equation (8)).

[33] The numerical experiments demonstrate how the vertical particle displacement profiles depend on the applied normal stress (Figure 8). In the simulations with low normal stress, a shear band develops at the top boundary and particle velocities decrease with depth. Due to the absence of a strong interparticle cohesion, the deformation accumulates

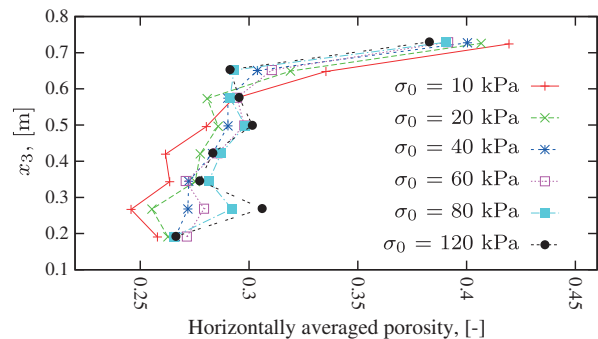


Figure 9. Porosity values of horizontally integrated slabs at the final time step in the numerical experiments.

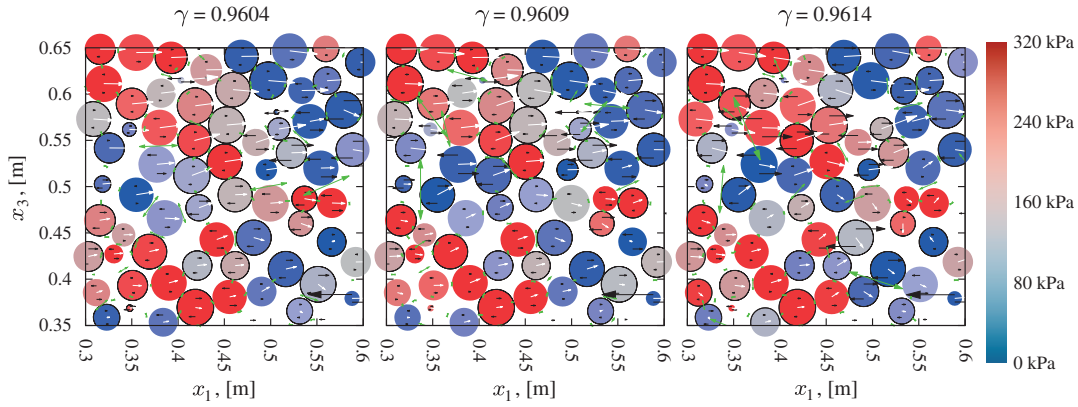


Figure 10. Particle kinematics inside the shear zone at three stages during the DEM experiment with $\sigma_0 = 80$ kPa. The particles are visualized as disks according to the intersection with the center (x_1, x_3) plane. The particle color corresponds to the contact pressure, rotational velocities are indicated using black arrows, linear velocities with white arrows, and interparticle slip velocities are shown with green arrows starting at the contact center. Particles spinning positively around the second axis are marked with a black border. It should be noted that with this type of planar visualization, the porosity appears larger than the true value and the spherical particles may be in physical contact although they appear not to be here. A supplementary animation is available at <http://users-cs.au.dk/adc/files/shear-80kPa-plane.mp4> (53 MB).

in shear bands of variable thickness instead of along sharp planes of failure [e.g., *Tchalenko, 1970*]. The shear zone thickness is equivalent to approximately seven mean particle diameters. For higher levels of normal stress, the deformation profile is deeper and the shear zone thicker. The internal porosity values (Figure 9) are strongly connected to the corresponding deformation profile (Figure 8), since shear strain in normally consolidated materials increases the porosity in the absence of particle crushing. Overall, the experiments with the lowest normal stress values have the highest porosity values in the upper zone of the material, which is a consequence of the shallow band of active deformation. The experiments with high normal stress values show a deeper increase of porosity, owing to the increased shear zone thickness. The shear zone itself displays a complex system of self-organized particle mechanics in highly transient patterns (Figure 10). The particle contact stresses result in rolling or interparticle slip, depending on which kinematic response requires the minimal amount of activation energy.

5. Discussion

5.1. Force Chains

[34] Granular materials are by definition heterogeneous, and the force network providing the stability of the system is nonuniform [*Jaeger et al., 1996*]. The force network is represented by the force chains that transmit stress through grain bridges or arches. Previous investigations have established that the mesh size of the force network has a characteristic size, about 10 times larger than the grain diameter, although sensitive to grain size variance [*Clement, 1999*]. It is likely that this length scale of the force network also defines the minimum thickness of shear zones.

[35] Our numerical experiments demonstrate that the force chains carry stress of high magnitude. Although particle breakage is not part of the modeling method, the DEM simulations hence support the hypothesis that force chains are effective mechanisms of grain crushing, even distant

from the rapidly deforming shear zones. Yet grain size modification due to particle abrasion is likely favored inside the shear zone, where the relative movement between particles is greatest. Grain bridges in till are mainly aligned oblique to the shear direction and are often associated with crushed grains [*Hooke and Iverson, 1995; Iverson et al., 1996; Larsen et al., 2007*]. *Hooke and Iverson [1995]* and *Iverson et al. [1996]* showed that failure of grains in force chain networks during shear significantly modifies the particle sizes, leading to a self-similar, fractal grain size distribution. As the grain sizes decrease, the finer components become more active in distributing stresses through the system. Since the mesh spacing in the stress network is a function of the typical grain size, the force chain distance decreases and the stress network becomes more homogeneous with less stress fluctuation [*Iverson et al., 1996; Morgan, 1999; Iverson, 2010*].

[36] The failure of force chains in a subglacial bed can be caused by particle crushing, particle rotation, interparticle sliding, or a change in the stress field, for instance induced by changes in subglacial hydrology. If the bed fails to establish a new force chain, exerting flow-resistant friction to the glacier base, the force chain failure can result in a propagating instability, possibly resulting in a glacial slip event. Clearly, the description of slip initiation and failure propagation in stress-limited systems requires more attention in future studies. A numerical DEM model, perhaps extended by angular particles for increased particle interlocking, is ideal for such studies, since it allows for a detailed quantification of the internal sediment mechanics at seismic time scales.

5.2. Variability of the Vertical Strain Distribution

[37] Our DEM simulations demonstrate a clear relationship between the applied normal stress and the depth of deformation (Figure 8). This result can be explained by considering the frictional strength of particle contacts. According to Mohr-Coulomb theory, the frictional strength of

particle contacts depends on pressure and force chain stability is therefore strengthened by high levels of normal stress. The strong force chains transmit stress over large distances, causing weak contact planes at greater depths to fail and the thickness of the deforming zone to increase.

[38] In situ measurements of subglacial water pressure [e.g., Engelhardt *et al.*, 1990; Murray and Clarke, 1995; Hooke *et al.*, 1997; Engelhardt and Kamb, 1997; Hart *et al.*, 2009; Bartholomaeus *et al.*, 2011] and sedimentary indications of palaeo-subglacial conditions [Piotrowski and Tulaczyk, 1999; Boyce and Eyles, 2000; Larsen *et al.*, 2004; Piotrowski *et al.*, 2001, 2006] show that the magnitude of the pore water pressure often lies close to the ice overburden pressure, modulated by diurnal and seasonal variations. In such cases, our numerical results suggest a deformation profile of convex shape (Figure 8). The subglacial transport rate of a warm-based glacier with a well-developed drainage system, resting on a granular bed, thus seems to be controlled by the value of the normal stress, the effective diameter of the granular material, and the basal velocity. The granular frictional mechanisms included here are, however, not sufficient to explain very thick deformation profiles, which may be due to thermal effects, ice-bed interface roughness, varying lithology, or hydrological feedbacks such as dilatant hardening [e.g., Iverson *et al.*, 1998; Evans *et al.*, 2006; Kjær *et al.*, 2006; Rathbun *et al.*, 2013]. However, the DEM results confirm that convex-upward displacement profiles are possible in Mohr-Coulomb granular materials, as also demonstrated by Tulaczyk *et al.* [2000] and Iverson and Iverson [2001].

5.3. Dynamics of Dilation and Porosity

[39] As a consequence of the relative movement of grains, normally consolidated granular materials initially dilate during shear [Reynolds, 1885]. The dilation stops when a critical stage is reached. Our numerical DEM setup behaves similarly. Furthermore, shifting configurations of the force chains cause frequent fluctuations of the DEM model thickness, although these are bound to decrease with increasing number of particles [Iverson *et al.*, 1996; Morgan, 1999; Li and Aydin, 2010].

[40] The implications of volumetric changes during shear band formation depend on the influence and properties of pore fluid flow. Importantly, the pore fluid can have two opposite effects, depending on the degree of grain crushing in the shear zone. Without significant grain crushing, the shear zone dilates under deformation. If the strain rate is sufficiently high, relative to the hydraulic permeability of the material, deformation decreases the local pore water pressure, which in turn increases the effective pressure. This increase in normal stress strengthens the material (equation (2)) and causes dilatant hardening [Iverson *et al.*, 1998]. Such hardening effects may drive migration of the shear zone. In contrast, shear zones may contract if grain crushing allows for repacking of the grains [Wafid *et al.*, 2004; Iverson *et al.*, 2010]. This contraction lowers the shear strength because of the pore water pressure increases (equation (2)). Furthermore, the fine-grained products of widespread grain crushing may accelerate this effect by decreasing the hydraulic conductivity and lowering the excess pore water pressure dissipation rate [Okada *et al.*, 2004; Iverson *et al.*, 2010]. The effect of such strain-induced softening is to stabilize the active shear zones.

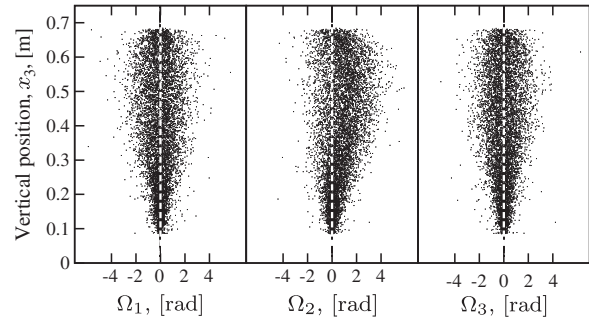


Figure 11. Scatterplots of the particle rotation, decomposed along each Euclidean axis. The results shown are from the last time step of the numerical DEM experiment with $\sigma_0 = 80$ kPa.

[41] In the absence of grain crushing and pore fluid transport, the DEM experiments indicate that the decrease of hydraulic pressure internally in the shear zone is a function of normal stress (Figure 9). A low level of normal stress results in the formation of a narrow shear zone with a highly reduced hydraulic pressure, whereas higher levels of normal stress result in a smaller pressure decrease. Still, the total deficit of hydraulic pressure is greater under high normal stress because it affects a much thicker zone (Figure 4, bottom). The effects of dilatant hardening are thus expected to be stronger under higher normal stresses.

[42] Our future numerical studies will focus on the mechanical interaction with a simulated pore fluid, by incorporating a full two-way coupling between pore fluid flow and the granular skeleton. This coupled methodology will allow small-scale investigations of the two-way interaction of moving grains and the interparticle fluid, even with complex geometries of the upper, moving boundary, such as during plowing [Tulaczyk *et al.*, 2001; Thomason and Iverson, 2008]. As highlighted by Iverson *et al.* [1998], the rheology of a grain-fluid mixture is likely to contain viscous components if the characteristic time scale for the diffusion of hydraulic pressures is smaller than the characteristic time scale for dilation.

5.4. Particle Rotation

[43] The particles in the numerical setup can have both translational and rotational movement components. Angular accelerations, velocities, and positions are handled as quaternions (three-dimensional rotation), whereby the direction of the quaternion denotes the rotational axis and the quaternion length relates to the rotation magnitude. The rotation follows the right-hand rule, implying that a particle with an angular velocity of $\omega = \{0, 1, 0\}$ rad s⁻¹ represents a rotation around the second axis, where the upper tangential velocity points in the positive direction of the first axis.

[44] Unidirectional rolling is assumed to dominate particle transport in the conceptual model of van der Meer [1997]. However, our DEM experiments demonstrate that particles in contact prefer to roll in opposite directions in order to avoid large contact slips (Figure 10). Since the tangential contact strength is scaled by the magnitude of the normal force (equation (8)), contacts between grains situated in a force chain are mechanically strong. For this reason, grains in force chains prefer to roll in opposite direction

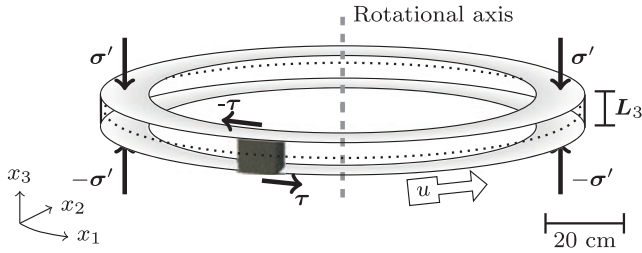


Figure 12. Geometry of the laboratory ring-shear apparatus sample chamber, which is filled with sediment during the shear tests. The dotted line marks the shearing gap in the side walls between the stationary upper loading platen and the lower mobile part.

in order to avoid slips, while slip on contacts in the adjacent, low-pressure areas are more frequent. During the small range of shear strain increments displayed in Figure 10, the stress-bearing force network is slightly relocated and several grains change rotational direction. This shows how the micromechanical system to a large extent reconfigures itself through a relatively small range of shear strain values. Yet it should be noted that the spheres of the numerical experiment likely favor rotation instead of slip, due to the absence of interlocking caused by grain angularity and elongation.

[45] The angular position can for each particle be calculated by integrating the rotational velocity, i.e., $\Omega^i = \int_0^t \omega^i dt$. For the experiment with $\sigma_0 = 80$ kPa, the estimated mean values of the total rotation per Euclidean axis are $\hat{\mu}(\Omega) = \{-0.0027, 0.50, -0.0053\}$ rad s^{-1} , with empirical variances of $s^2(\Omega) = \{0.76, 1.1, 0.68\}$ (Figure 11). These results illustrate that the mean direction of the rotational axes has a strain signature and that this trend in rotational direction is already developed at a shear strain of $\gamma = 1$. The relatively large variance values indicate, however, that rotational microstructures are to be expected in any orientation. The direction of shear strain can thus theoretically be deduced only from a very large data set of rotational axis orientations. Rotational structures are often very abundant in tills [e.g., *van der Meer*, 1993; *Menzies*, 2000; *Hiemstra and Rijdsdijk*, 2003], and they have been identified in thin sections both parallel and perpendicular to the shear stress direction, suggesting that they may form in various stress regimes and with an inherent variability in the orientation of the rotational axes.

5.5. Comparison to Laboratory Ring-Shear Experiments

[46] Ring-shear machines have previously been used to investigate the mechanical behavior of till [e.g., *Iverson et al.*, 1996, 1997, 1998; *Tulaczyk et al.*, 2000; *Müller and Schlüchter*, 2000; *Moore and Iverson*, 2002] and the development of strain signatures [e.g., *Iverson et al.*, 1996, 1997; *Hooyer and Iverson*, 2000a, 2000b; *Müller and Schlüchter*, 2000; *Thomason and Iverson*, 2006; *Larsen et al.*, 2006; *Iverson et al.*, 2008]. Here stress measurements from ring-shear experiments are compared to the simulated DEM granular behavior. Our ring-shear apparatus (Figure 12) (see also *Larsen et al.* [2006] and *Bateman et al.* [2012]) has a sample chamber volume of 14480 cm³, a chamber width of 12.0 cm, and a chamber height of 8.0 cm.

The centerline diameter is 54.0 cm. The upper platen is rotationally fixed, while the lower platen is moved at a constant velocity ($u = 1.67 \times 10^{-5}$ m $s^{-1} = 1.0$ mm min^{-1}). To quantify the distribution of strain, we inserted coarse (2–4 mm), angular quartz and feldspar grains as strain markers.

[47] The geometry of the numerical setup (Figure 3) and the ring-shear apparatus (Figure 12) both allow infinite shear strains, owing to the absence of boundaries in the shear direction. On the other hand, factors that are likely to produce significant differences between laboratory and numerical experiments are associated with side wall friction in the ring-shear sample chamber, the elastic response and acceleration of the mechanical parts in the ring-shear apparatus, and the difference in particle numbers.

[48] In order to provide a wide framework for comparison, we performed laboratory experiments with several types of materials. The first material consisted of spherical glass beads with a mean grain size of approximately 4.0×10^{-4} m (best fitted with a log-normal distribution with $\mu = -5.5$ and $\sigma = 0.21$). The second material used was an industrially sorted, angular to subangular, aeolian quartz sand, also with a mean grain size of approximately 4.0×10^{-4} m (best log-normal fit with $\mu = -5.5$ and $\sigma = 0.26$).

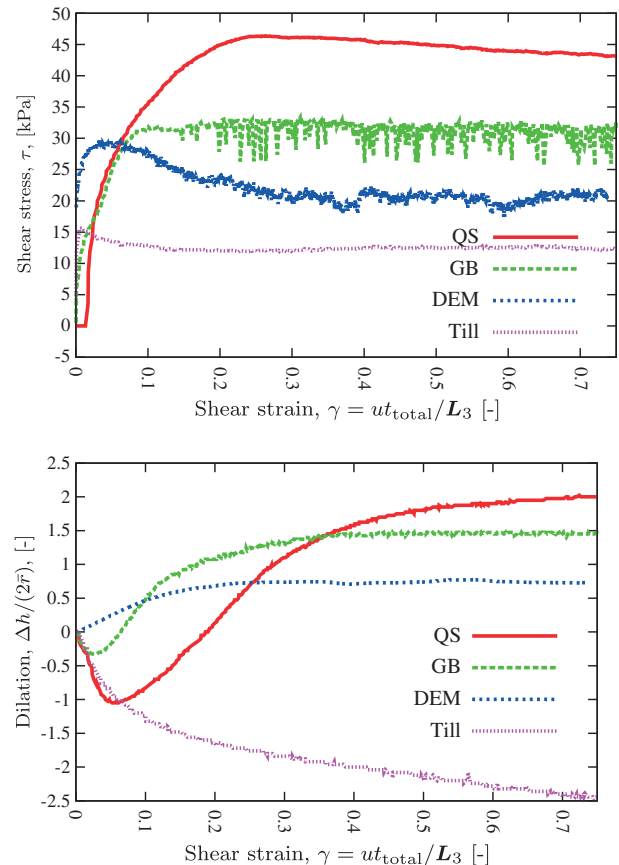


Figure 13. (top) Shear stress and (bottom) dilation as a function of shear strain, recorded during the laboratory shear tests on quartz sand (QS), glass beads (GB), till, and the numerical discrete element method material (DEM). The normal stress is $\sigma_0 = 80$ kPa for all tests, except for the till, where $\sigma_0 = 85$ kPa. The till shear stress values are scaled to account for the differences in normal stress.

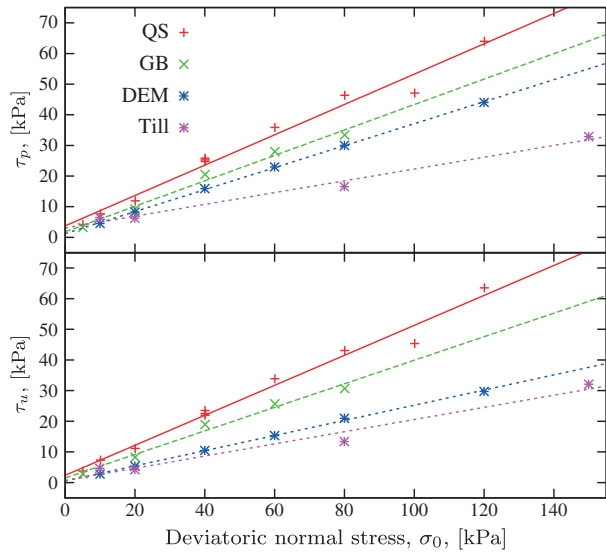


Figure 14. Mohr-Coulomb failure analysis of three laboratory granular materials and one numerical material. Equation (2) was fitted to the $(\sigma_0, \tau_{p,u})$ data sets using the nonlinear least squares Marquardt-Levenberg algorithm. (top) Peak shear strength values (τ_p). (bottom) Ultimate shear strength values (τ_u).

The experiments on these materials were performed under dry conditions. Also used for the comparison study was a previous Mohr-Coulomb failure analysis on a Weichselian-age basal till from the Scandinavian Ice Sheet [Tylmann *et al.*, 2013], performed in the same ring-shear apparatus. The till was sheared under water-saturated conditions with a hydrological connection through filters in the chamber top and bottom to atmospheric pressure. The till was poorly sorted with a bimodal grain size distribution with peaks in the sand and silt fractions.

[49] We use the laboratory results to compare the simulated DEM granular behavior with that of real materials under similar conditions. Due to the side wall friction, the magnitude of the material shear strength is likely to be higher in the laboratory materials. We can, however, compare the stress-strain dynamics observed by the two methods (Figure 13) and attempt to explain the differences in the material behavior (Figure 14 and Table 2), bearing in mind the aforementioned caveats.

[50] The shearing of a granular material from a prefailure, normal consolidated state can be subdivided into multiple stages [cf. Li and Aydin, 2010], which we recognize in both the laboratory and the numerical settings:

[51] 1. stage: The initial shearing motion results in contraction, caused by the combined effect of increased elastic deformation, and reorganization of the grains. Both effects are caused by the increased magnitude and reorientation of the maximum compressive stress ($\sigma' + \tau$). The increase in maximum compressive stress promotes consolidation and decreases porosity [Nedderman, 1992; Tulaczyk *et al.*, 2000]. The elastic response is increased if the grains are angular, which can stabilize the intergrain contacts mechanically [Nedderman, 1992; Weatherley *et al.*, 2012]. The numerical DEM material does not exhibit contraction during stage 1 shear, since particles are spherical and for this

reason cannot develop interlocking. The glass beads and the quartz sand both display a transient contraction during this stage. Owing to the angularity of grains, the quartz sand displays the strongest contraction and the longest duration of this stage.

[52] 2. stage: The material dilates due to relative particle movement [Reynolds, 1885; Mead, 1925] and exhibits its peak shear strength value (τ_p). The shear zone evolves into a high-porosity layer [de Gennes, 1999]. The numerical material, the glass beads, and the quartz sand dilate during this stage. The numerical material dilates to approximately 0.75 grain diameters, the glass beads dilate to 1.5 grain diameters, the quartz sand to 2.0 grain diameters. The till continues to contract. This contraction is caused by the volumetric decrease due to microfabric and macrofabric development and subsequent diffusion of the increased internal hydraulic pressures. In addition to this, a small volume of till was after the experiments observed to having been squeezed out of the sample chamber.

[53] 3. stage: In the final stage, the shear zone becomes fully developed, as the material reaches the critical state. The shear strength decreases to the ultimate value (τ_u) and dilation stops [Schofield and Wroth, 1968]. This behavior is observed in the numerical material, the quartz sand, and the till. The materials display no low-frequency volumetric and shear strength changes, only high-frequency fluctuations caused by fracturing of the grains or reorganization of the internal force-bearing network [Iverson *et al.*, 1996; Li and Aydin, 2010]. As observed in similar experiments [Mair *et al.*, 2002], the glass beads show stick-slip behavior at this stage, owing to elasticity of the apparatus. No measurable products of grain crushing are detected, which rules out fracturing of grains as the cause of the fluctuations.

5.5.1. Particle Shape and Angularity

[54] Comparing the stress-strain relationships of the DEM and the laboratory materials highlights the importance of grain shape and angularity for the macroscopical geotechnical behavior. The initial elastic response, the peak shear strength, and the total dilation are all higher in the materials with angular grains, such as the quartz sand. The spherical materials, such as the glass beads and the numerical DEM particles, are mechanically weaker and show lower values of dilation. For a normal stress of 80 kPa, the shear zone is approximately 4 mm thick in the glass beads and 6 mm thick in the quartz sand. As demonstrated by Mueth *et al.* [2000], spherical and smooth particles generally exhibit deformation in narrow shear bands. The shear strength of materials tends to increase with grain angularity [e.g., Mair *et al.*, 2002; Anthony and Marone, 2005; Azéma *et al.*, 2012]. The shear strength also tends to increase with grain elongation [Azéma and Radjai, 2010], which is a prerequisite for fabric development [Hooyer and Iverson, 2000a; Mair *et al.*,

Table 2. Fitted Values of the Mohr-Coulomb Relationship (Equation (2)) at the Peak (p) and Ultimate (u) Failure Stages of the Materials

Material	ϕ_p [°]	C_p [kPa]	ϕ_u [°]	C_u [kPa]
Quartz sand	45	3.7	44	2.4
Glass beads	37	1.8	35	1.5
DEM	32	1.2	22	0.51
Till	18	3.1	18	0.69

2002; Thomason and Iverson, 2006]. Therefore, the simplified grain shape in the DEM relative to real materials evidently influences the levels of stress and dilation. Still, the Mohr-Coulomb model is equally valid for the numerical and laboratory materials.

[55] Future studies will focus on expanding the numerical method to simulate interparticle bonds [Potyondy and Cundall, 2004; Wang et al., 2006; Wang, 2009; Obermayr et al., 2012]. With particle bonds, it is possible to include irregularly shaped, breakable aggregates of bonded spheres. By simulating angular particle clusters instead of loose spheres, the initial, low-strain elastic response during stage I shear may be improved due to greater interlocking of particles inside force chains, which is likely to increase the material shear strength. The bond functionality will also enable studies of fabric development and modifications of grain size distribution during progressive shear.

5.5.2. Particle Size Distribution and Mineralogy

[56] In comparison to the DEM, the laboratory materials contain a wider range of particle sizes. Morgan and Boettcher [1999] showed that in two-dimensional shear experiments with a variety of grain size distributions, the presence of fine particles caused strain localization, which is consistent with the theory of the shear zone thickness being a function of the grain size [de Gennes, 1999; Herrmann, 2001]. Mair et al. [2002] demonstrated no significant shear strength differences between narrow and wide grain size distributions of spherical glass beads, whereas Morgan [1999] reported a slight shear strength decrease with the volumetric increase of fine, but micromechanically identical particles.

[57] Clay minerals are known to behave differently than coarser granulates, and a high clay content may therefore influence the macromechanical material behavior significantly [Iverson et al., 1997]. Often, shear zones in clay are more narrow due to the smaller grain size, and cohesion causes clays to deform by both folding and faulting and fracturing [Eisenstadt and Sims, 2005]. Clay particles interact not only with mechanical repulsion upon contact but with a variety of physicochemical interactions causing repulsion and attraction at different spatial configurations. Yao and Anandarajah [2003] introduced a methodology for simulating clay minerals in DEM models, which will serve as a basis for future quantification of the role of clays in glacial diamicts.

6. Conclusions

[58] The discrete element method, although parameterized by micromechanical properties, is useful for modeling the macroscopic mechanical properties of simple granular materials, sheared under dry conditions. The concept of a numerical DEM model may complement analog experiments, since it allows a detailed investigation of the microphysics. The DEM displays dilation during deformation and self-organizing particle kinematics. Both effects are difficult to capture in conventional numerical models based on continuum mechanics. From numerical shear experiments, we show how relatively high values of normal overburden stress result in deep, distributed profiles of deformation and a thick zone of increased porosity. A lower overburden stress results in relatively narrow boundary layers of deformation that are characterized by high porosity. Our DEM experiments

demonstrate how stress in a granular material is heterogeneously distributed along force-bearing particle chains. The force chains are transient in nature, but the mean orientation of the load-bearing contacts is clearly governed by the direction of the maximum compressive stress. We suggest that the transient stability of the force chains represents an important aspect of subglacial sediment deformation. Particle rotational axes tend to align with progressive shear, although closer examination shows that particles in contact often rotate in opposite directions in order to avoid slip along the interparticle contact interfaces.

[59] **Acknowledgments.** We thank the laboratory staff at the Department of Geoscience, Aarhus University for performing grain size analyses and assisting during the laboratory experiments. We thank Neal Iverson, Jason Thomason, and an anonymous reviewer for constructive reviews, which improved the quality of the manuscript. This research was funded by the Danish Council for Independent Research under the Sapere Aude programme. S. Tulaczyk's involvement in this research was supported by NSF-ANT-0839142, and K. Tylmann was funded by NSC grant 2011/01/N/ST/10/05880.

References

- Aharonov, E., and D. Sparks (2002), Shear profiles and localization in simulations of granular shear, *Phys. Rev. E*, *65*, 051302.
- Alley, R. B., D. D. Blankenship, C. R. Bentley, and S. T. Rooney (1986), Deformation of till beneath ice stream B, West Antarctica, *Nature*, *322*, 57–59.
- Alley, R. B., D. D. Blankenship, S. T. Rooney, and C. R. Bentley (1987), Till beneath ice stream B 4. A coupled ice-till flow model, *J. Geophys. Res.*, *92*(B9), 8931–8940.
- Anthony, J. L., and C. Marone (2005), Influence of particle characteristics on granular friction, *J. Geophys. Res.*, *110*(B8), B08409, doi:10.1029/2004JB003399.
- Atkinson, J. H., and P. L. Bransby (1979), *The Mechanics of Soils: An Introduction to Critical State Soil Mechanics*, pp. 124, McGraw Hill, New York.
- Azéma, E., and F. Radjai (2010), Stress-strain behavior and geometrical properties of packings of elongated particles, *Phys. Rev. E*, *81*, 051304.
- Azéma, E., N. Estrada, and F. Radjai (2012), Nonlinear effects of particle shape angularity in sheared granular media, *Phys. Rev. E*, *86*, 041301.
- Bartholomaeus, T. C., R. S. Anderson, and S. P. Anderson (2011), Growth and collapse of the distributed subglacial hydrologic system of Kennicott Glacier, Alaska, USA, and its effects on basal motion, *J. Glaciol.*, *57*(206), 985.
- Bateman, M. D., D. A. Swift, J. A. Piotrowski, and D. C. W. Sanderson (2012), Investigating the effects of glacial shearing of sediment on luminescence, *Quat. Geochronol.*, *10*, 230–236.
- Belheine, N., J. P. Plassiard, F.-V. Donzé, F. Darve, and A. Seridi (2009), Numerical simulation of drained triaxial test using 3D discrete element modeling, *Comput. Geotech.*, *36*(1), 320–331.
- Bougamont, M., and P. Christoffersen (2012), Hydrologic forcing of ice stream flow promotes rapid transport of sediment in basal ice, *Geology*, *40*(8), 735–738.
- Bougamont, M., S. Price, P. Christoffersen, and A. J. Payne (2011), Dynamic patterns of ice stream flow in a 3-D higher-order ice sheet model with plastic bed and simplified hydrology, *J. Geophys. Res.*, *116*, F04018, doi:10.1029/2011JF002025.
- Boulton, G. S. (1996), Theory of glacial erosion, transport and deposition as a consequence of subglacial sediment deformation, *J. Glaciol.*, *42*(140), 43–62.
- Boulton, G. S., and R. C. A. Hindmarsh (1987), Sediment deformation beneath glaciers: Rheology and geological consequences, *J. Geophys. Res.*, *92*(B9), 9059–9082.
- Boulton, G. S., and A. S. Jones (1979), Stability of temperate ice caps and ice sheets resting on beds of deformable sediment, *J. Glaciol.*, *24*(90), 29–43.
- Boyce, J. I., and N. Eyles (2000), Architectural element analysis applied to glacial deposits: Internal geometry of a late Pleistocene till sheet, Ontario, Canada, *Geol. Soc. Am. Bull.*, *112*(1), 98–118.
- Bueler, E., and J. Brown (2009), Shallow shelf approximation as a “sliding law” in a thermomechanically coupled ice sheet model, *J. Geophys. Res.*, *114*(F3), F03008, doi:10.1029/2008JF001179.
- Campbell, C. S. (2006), Granular material flows – An overview, *Powder Technol.*, *162*, 208–229.

- Cheng, Y. P., Y. Nakata, and M. D. Bolton (2003), Discrete element simulation of crushable soil, *Geotechnique*, 53(7), 633–642.
- Clarke, G. K. C. (2005), Subglacial processes, *Annu. Rev. Earth Planet. Sci.*, 33, 247–276.
- Clarke, G. K. C., S. G. Collins, and D. E. Thompson (1984), Flow, thermal structure, and subglacial conditions of the surge-type glacier, *Can. J. Earth Sci.*, 21(2), 232–240.
- Clement, E. (1999), Rheology of granular media, *Curr. Opin. Colloid Interface Sci.*, 4(4), 294–299.
- Cuffey, K. M., and W. S. B. Paterson (2010), *The Physics of Glaciers*, 4th ed., vol. 4, pp. 693, Academic Press, Elsevier.
- Cundall, P. A., and O. D. L. Strack (1979), A discrete numerical model for granular assemblies, *Geotechnique*, 29, 47–65.
- de Borst, R. (1991), Numerical modelling of bifurcation and localisation in cohesive-frictional materials, *Pure Appl. Geophys.*, 137(4), 367–390.
- de Gennes, P. G. (1999), Granular matter: A tentative view, *Rev. Mod. Phys.*, 71(2), 374–382.
- Drake, T. G., and J. Calantoni (2001), Discrete particle model for sheet flow sediment transport, *J. Geophys. Res.*, 106, 19–859.
- Egholm, D. L., M. Sandiford, O. R. Clausen, and S. B. Nielsen (2007), A new strategy for discrete element numerical models. 2. Sandbox applications, *J. Geophys. Res.*, 112, B05204, doi:10.1029/2006JB004558.
- Egholm, D. L., O. R. Clausen, M. Sandiford, M. B. Kristensen, and J. A. Korstgård (2008), The mechanics of clay smearing along faults, *Geology*, 36(10), 787–790.
- Eisenstadt, G., and D. Sims (2005), Evaluating sand and clay models: Do rheological differences matter?, *J. Struct. Geol.*, 27, 1399–1412.
- Engelhardt, H., and B. Kamb (1997), Basal hydraulic system of a West Antarctic ice stream: Constraints from borehole observations, *J. Glaciol.*, 43(144), 207–230.
- Engelhardt, H., N. Humphrey, B. Kamb, and M. Fahnestock (1990), Physical conditions at the base of a fast moving Antarctic ice stream, *Science*, 248(4951), 57–59.
- Evans, D. J. A., and B. R. Rea (1999), Geomorphology and sedimentology of surging glaciers: A land-systems approach, *Ann. Glaciol.*, 28(1), 75–82.
- Evans, D. J. A., E. R. Phillips, J. F. Hiemstra, and C. A. Auton (2006), Subglacial till: Formation, sedimentary characteristics and classification, *Earth Sci. Rev.*, 78(1-2), 115–176.
- Fowler, A. C. (2000), An instability mechanism for drumlin formation, *J. Geol. Soc. London*, 176(1), 307–319.
- Fowler, A. C. (2003), On the rheology of till, *Ann. Glaciol.*, 37(1), 55–59.
- Fraige, F. Y., and P. A. Langston (2004), Integration schemes and damping algorithms in distinct element models, *Adv. Powder Technol.*, 15(2), 227–245.
- Hart, J. K., K. C. Rose, K. Martinez, and R. Ong (2009), Subglacial clast behaviour and its implication for till fabric development: New results derived from wireless subglacial probe experiments, *Quat. Sci. Rev.*, 28(7-8), 597–607.
- Herrmann, H. (2001), Structures in deformed granular packings, *Granular Matter*, 3(1), 15–18.
- Herrmann, H. J. (2002), Granular matter, *Physica A*, 313(1-2), 188–210.
- Hiemstra, J. F., and K. F. Rijdsdijk (2003), Observing artificially induced strain: Implications for subglacial deformation, *J. Quaternary Sci.*, 18(5), 373–383.
- Hindmarsh, R. C. A. (1998), The stability of a viscous till sheet coupled with ice flow, considered at wavelengths less than the ice thickness, *J. Glaciol.*, 44(147), 285–292.
- Hinrichsen, H., and D. E. Wolf (2006), *The Physics of Granular Media*, Wiley, New York.
- Hooke, R. L. B., and N. R. Iverson (1995), Grain-size distribution in deforming subglacial tills: Role of grain fracture, *Geology*, 23(1), 57–60.
- Hooke, R. L. B., B. Hanson, N. R. Iverson, P. Jansson, and U. Fischer (1997), Rheology of till beneath Storglaciären, Sweden, *J. Glaciol.*, 43(143), 172–179.
- Hooyer, T. S., and N. R. Iverson (2000a), Diffusive mixing between shearing granular layers: Constraints on bed deformation from till contacts, *J. Glaciol.*, 46(155), 641–651.
- Hooyer, T. S., and N. R. Iverson (2000b), Clast-fabric development in a shearing granular material: Implications for subglacial till and fault gouge, *Geol. Soc. Am. Bull.*, 112(5), 683.
- Iverson, N. R. (2010), Shear resistance and continuity of subglacial till: Hydrology rules, *J. Glaciol.*, 56(200), 1104–1114.
- Iverson, N. R., J. E. Mann, and R. M. Iverson (2010), Effects of soil aggregates on debris-flow mobilization: Results from ring-shear experiments, *Eng. Geol.*, 114, 84–92.
- Iverson, N. R., and R. M. Iverson (2001), Distributed shear of subglacial till due to Coulomb slip, *J. Glaciol.*, 47(158), 481–488.
- Iverson, N. R., T. S. Hooyer, and R. L. B. Hooke (1996), A laboratory study of sediment deformation: Stress heterogeneity and grain-size evolution, *Ann. Glaciol.*, 22, 167–175.
- Iverson, N. R., R. W. Baker, and T. S. Hooyer (1997), A ring-shear device for the study of till deformation: Tests on tills with contrasting clay contents, *Quat. Sci. Rev.*, 16(9), 1057–1066.
- Iverson, N. R., T. S. Hooyer, and R. W. Baker (1998), Ring-shear studies of till deformation: Coulomb-plastic behavior and distributed strain in glacier beds, *J. Glaciol.*, 148, 634–642.
- Iverson, N. R., T. S. Hooyer, J. F. Thomason, M. Graesch, and J. R. Shumway (2008), The experimental basis for interpreting particle and magnetic fabrics of sheared till, *Earth Surf. Processes Landforms*, 33(4), 627–645.
- Jaeger, H. M., S. R. Nagel, and R. P. Behringer (1996), Granular solids, liquids, and gases, *Rev. Mod. Phys.*, 68(4), 1259–1273.
- Kamb, B. (1991), Rheological nonlinearity and flow instability in the deforming bed mechanism of ice stream motion, *J. Geophys. Res.*, 96(B10), 16,585–16,595.
- Kirk, D. B., and W.-M. Hwu (2010), *Programming Massively Parallel Processors*, Morgan Kaufmann Publishers, San Francisco, CA, USA.
- Kjær, K. H., E. Larsen, J. van der Meer, Ö. Ingólfsson, J. Krüger, Í. Örn Benediktsson, C. G. Knudsen, and A. Schomacker (2006), Subglacial decoupling at the sediment/bedrock interface: A new mechanism for rapid flowing ice, *Quat. Sci. Rev.*, 25(21), 2704–2712.
- Krimer, D. O., S. Mahle, and M. Liu (2012), Dip of the granular shear stress, *Phys. Rev. E*, 86(6), 061312.
- Krugger-Emden, H., M. Sturm, S. Wirtz, and V. Scherer (2008), Selection of an appropriate time integration scheme for the discrete element method (DEM), *Comput. Chem. Eng.*, 32(10), 2263–2279.
- Kudrolli, A. (2004), Size separation in vibrated granular matter, *Rep. Prog. Phys.*, 67, 209.
- Larsen, N. K., J. A. Piotrowski, and C. Kronborg (2004), A multiproxy study of a basal till: A time-transgressive accretion and deformation hypothesis, *J. Quaternary Sci.*, 19(1), 9–21.
- Larsen, N. K., J. A. Piotrowski, and F. Christiansen (2006), Microstructures and microshears as proxy for strain in subglacial diamicts: Implications for basal till formation, *Geology*, 34(10), 889.
- Larsen, N. K., J. A. Piotrowski, and J. Menzies (2007), Microstructural evidence of low-strain, time-transgressive subglacial deformation, *J. Quaternary Sci.*, 22(6), 593–608.
- Li, Y. R., and A. Aydin (2010), Behavior of rounded granular materials in direct shear: Mechanisms and quantification of fluctuations, *Eng. Geol.*, 115(1-2), 96–104.
- Mair, K., K. M. Frye, and C. Marone (2002), Influence of grain characteristics on the friction of granular shear zones, *J. Geophys. Res.*, 107(B10), 2219, doi:10.1029/2001JB000516.
- Mair, K., and S. Abe (2008), 3D numerical simulations of fault gouge evolution during shear: Grain size reduction and strain localization, *Earth Planet. Sci. Lett.*, 274(1-2), 72–81.
- Mead, W. J. (1925), The geologic role of dilatancy, *J. Geol.*, 33(7), 685–698.
- GDR-MiDi (2004), On dense granular flows, *Eur. Phys. J. E*, 14, 341–365.
- Menzies, J. (2000), Micromorphological analyses of microfibrils and microstructures indicative of deformation processes in glacial sediments, *Geol. Soc. Spec. Publ.*, 176(1), 245–257.
- Moore, P. L., and N. R. Iverson (2002), Slow episodic shear of granular materials regulated by dilatant strengthening, *Geology*, 30(9), 843–846.
- Morgan, J. K. (1999), Numerical simulations of granular shear zones using the distinct element method: 2. Effects of particle size distribution and interparticle friction on mechanical behavior, *J. Geophys. Res.*, 104(B2), 2721–2732.
- Morgan, J. K. (2004), Particle dynamics simulations of rate- and state-dependent frictional sliding of granular fault gouge, *Pure Appl. Geophys.*, 161(9), 1877–1891.
- Morgan, J. K., and M. S. Boettcher (1999), Numerical simulations of granular shear zones using the distinct element method: 1. Shear zone kinematics and the micromechanics of localization, *J. Geophys. Res.*, 104(B2), 2703–2719.
- Mueth, D. M., G. F. Debregeas, G. S. Karczmar, P. J. Eng, S. R. Nagel, and H. M. Jaeger (2000), Signatures of granular microstructure in dense shear flows, *Nature*, 406(6794), 385–389.
- Müller, B. U., and C. Schlüchter (2000), Influence of the glacier bed lithology on the formation of a subglacial till sequence—ring-shear experiments as a tool for the classification of subglacial tills, *Quat. Sci. Rev.*, 20(10), 1113–1125.
- Murray, T., and G. K. C. Clarke (1995), Black-box modeling of the subglacial water system, *J. Geophys. Res.*, 100(B6), 10,231–10,245.
- Murray, T., G. W. Stuart, P. J. Miller, J. Woodward, A. M. Smith, P. R. Porter, and H. Jiskoot (2000), Glacier surge propagation by thermal evolution, *J. Geophys. Res.*, 105(B6), 13–491.

- Murray, T., T. Strozzi, A. Luckman, H. Jiskoot, and P. Christakos (2003), Is there a single surge mechanism? Contrasts in dynamics between glacier surges in Svalbard and other regions, *J. Geophys. Res.*, *108*(B5), 2237, doi:10.1029/2002JB001906.
- Nedderman, R. M. (1992), *Statics and Kinematics of Granular Materials*, Cambridge Univ. Press, Cambridge.
- Ng, F. S. L. (2000), Coupled ice-till deformation near subglacial channels and cavities, *J. Glaciol.*, *46*(155), 580–598.
- NVIDIA (2013a), *CUDA, C Programming Guide*, 5.0 ed., NVIDIA Corporation: Santa Clara, CA, USA.
- NVIDIA (2013b), *CUDA, C Best Practices Guide Version*, 5.0 ed., NVIDIA Corporation: Santa Clara, CA USA.
- Nygård, A., H. P. Sejrup, H. Hafidason, W. A. H. Lekens, C. D. Clark, and G. R. Bigg (2007), Extreme sediment and ice discharge from marine-based ice streams: New evidence from the North Sea, *Geology*, *35*(5), 395–398.
- Obermayr, M., K. Dressler, C. Vrettos, and P. Eberhard (2012), A bonded-particle model for cemented sand, *Comput. Geotech.*, *49*, 299–313.
- Okada, Y., K. Sassa, and H. Fukuoka (2004), Excess pore pressure and grain crushing of sands by means of undrained and naturally drained ring-shear tests, *Eng. Geol.*, *75*(3-4), 325–343.
- O'Sullivan, C., and J. D. Bray (2004), Selecting a suitable time step for discrete element simulations that use the central difference time integration scheme, *Eng. Computation.*, *21*(2/3/4), 278–303.
- Phillips, E., J. Everest, and H. Reeves (2013), Micromorphological evidence for subglacial multiphase sedimentation and deformation during overpressurized fluid flow associated with hydrofracturing, *Boreas*, *42*, 395–427.
- Piotrowski, J. A., and S. Tulaczyk (1999), Subglacial conditions under the last ice sheet in northwest Germany: Ice-bed separation and enhanced basal sliding?, *Quat. Sci. Rev.*, *18*(6), 737–751.
- Piotrowski, J. A., D. M. Mickelson, S. Tulaczyk, D. Krzyszkowski, and F. D. Junge (2001), Were deforming subglacial beds beneath past ice sheets really widespread? *Quat. Int.*, *86*(1), 139–150.
- Piotrowski, J. A., N. K. Larsen, J. Menzies, and W. Wysota (2006), Formation of subglacial till under transient bed conditions: Deposition, deformation, and basal decoupling under a Weichselian ice sheet lobe, central Poland, *Sedimentology*, *53*(1), 83–106.
- Potyondy, D. O., and P. A. Cundall (2004), A bonded-particle model for rock, *Int. J. Rock Mech. Min. Sci.*, *41*(8), 1329–1364.
- Rathbun, A. P., F. Renard, and S. Abe (2013), Numerical investigation of the interplay between wall geometry and friction in granular fault gouge, *J. Geophys. Res. Solid Earth*, *118*(3), 878–896, doi:10.1002/jgrb.50106.
- Rathbun, A. P., C. Marone, R. B. Alley, and S. Anandakrishnan (2008), Laboratory study of the frictional rheology of sheared till, *J. Geophys. Res.*, *113*(F2), F02020, doi:10.1029/2007JF000815.
- Reynolds, O. (1885), On the dilatancy of media composed of rigid particles in contact, *Phil. Mag.*, *20*(5), 46.
- Rosato, A. D., D. L. Blackmore, N. Zhang, and Y. Lan (2002), A perspective on vibration-induced size segregation of granular materials, *Chem. Eng. Sci.*, *57*(2), 265–275.
- Rudnicki, J. W., and J. R. Rice (1975), Conditions for the localization of the deformation in pressure-sensitive dilatant materials, *J. Mech. Phys. Solids*, *23*, 371–394.
- Schofield, A. N., and P. Wroth (1968), *Critical State Soil Mechanics*, McGraw-Hill, London.
- Schoof, C. (2006), A variational approach to ice stream flow, *J. Fluid Mech.*, *556*(1), 227–251.
- Sun, Q., G. Wang, and Y. Xu (2001), DEM applications to aeolian sediment transport and impact process in saltation, *Part. Sci. Technol.*, *19*(4), 339–353.
- Tchalenko, J. S. (1970), Similarities between shear zones of different magnitudes, *Geol. Soc. Am. Bull.*, *81*(6), 1625–1640.
- Thomason, J. F., and N. R. Iverson (2006), Microfabric and microshear evolution in deformed till, *Quat. Sci. Rev.*, *25*(9-10), 1027–1038.
- Thomason, J. F., and N. R. Iverson (2008), A laboratory study of particle ploughing and pore-pressure feedback: A velocity-weakening mechanism for soft glacier beds, *J. Glaciol.*, *54*(184), 169–181.
- Tulaczyk, S. (1999), Ice sliding over weak, fine-grained tills: Dependence of ice-till interactions on till granulometry, *Geol. Soc. Am. S.*, *337*, 159–177.
- Tulaczyk, S. (2006), Scale independence of till rheology, *J. Glaciol.*, *52*(178), 377–380.
- Tulaczyk, S., W. B. Kamb, and H. F. Engelhardt (2000), Basal mechanics of ice stream B, West Antarctica: 1. Till mechanics, *J. Geophys. Res.*, *105*(B1), 463–481.
- Tulaczyk, S. M., R. P. Scherer, and C. D. Clark (2001), A ploughing model for the origin of weak tills beneath ice streams: A qualitative treatment, *Quat. Int.*, *86*(1), 59–70.
- Tylmann, K., J. A. Piotrowski, and W. Wysota (2013), The ice/bed interface mosaic: Deforming spots intervening with stable areas under the fringe of the Scandinavian Ice Sheet at Samplawa, Poland, *Boreas*, *42*(2), 428–441.
- van der Meer, J. (1993), Microscopic evidence of subglacial deformation, *Quat. Sci. Rev.*, *12*(7), 553–587.
- van der Meer, J. (1996), Micromorphology, in *Past Glacial Environments: Sediments Forms and Techniques*, edited by J. Menzies, pp. 335–355, Butterworth-Heinemann, Oxford, U. K.
- van der Meer, J. (1997), Particle and aggregate mobility in till: Microscopic evidence of subglacial processes, *Quat. Sci. Rev.*, *16*(8), 827–831.
- Vaughan-Hirsch, D., E. Phillips, J. R. Lee, and J. K. Hart (2013), Micromorphological analysis of poly-phase deformation associated with the transport and emplacement of glaciotectionic rafts at West Runton, north Norfolk, UK, *Boreas*, *42*, 376–394.
- Wafid, M., K. Sassa, H. Fukuoka, and G. Wang (2004), Evolution of shear-zone structure in undrained ring-shear tests, *Landslides*, *1*(2), 101–112.
- Wang, Y. (2009), A new algorithm to model the dynamics of 3-D bonded rigid bodies with rotations, *Acta Geotechnica*, *4*(2), 117–127.
- Wang, Y., S. Abe, S. Latham, and P. Mora (2006), Implementation of particle-scale rotation in the 3-D lattice solid model, *Pure Appl. Geophys.*, *163*(9), 1769–1785.
- Weatherley, D., B. Wruck, W. Hancock, and G. P. Chitombo (2012), Investigations on comminution of sheared prismatic granular materials using the discrete element method, Geophysical Research Abstracts EGU2012-8333, vol. 14, presented at EGU General Assembly, held April 22-27, 2012 in Vienna, Austria.
- Yao, M., and A. Anandarajah (2003), Three-dimensional discrete element method of analysis of clays, *J. Eng. Mech.*, *129*(6), 585–596.
- Yohannes, B., L. Hsu, W. E. Dietrich, and K. M. Hill (2012), Boundary stresses due to impacts from dry granular flows, *J. Geophys. Res.*, *117*(F2), F02027, doi:10.1029/2011JF002150.
- Zhang, Y., and C. S. Campbell (1992), The interface between fluid-like and solid-like behaviour in two-dimensional granular flows, *J. Fluid Mech.*, *237*, 541.